

Population inversion in Landau-quantized graphene

Florian Wendler* and Ermin Malic

*Institute of Theoretical Physics, Nonlinear Optics and Quantum Electronics,
Technical University Berlin, Hardenbergstrasse 36, Berlin 10623, Germany.*

Landau level lasers have the advantage of tunability of the laser frequency by means of the external magnetic field. The crucial prerequisite of such a laser is a population inversion between optically coupled Landau levels. Efficient carrier-carrier and carrier-phonon scattering generally suppresses this effect in conventional materials. Based on microscopic calculations, we predict for the first time the occurrence of a long-lived population inversion in Landau-quantized graphene and reveal the underlying many-particle mechanisms. To guide the experimental demonstration, we present optimal conditions for the observation of a maximal population inversion in terms of experimentally accessible parameters, such as the strength of the magnetic field, pump fluence, temperature, and doping. We reveal that in addition to the tunability of the Landau-level laser frequency, also the polarization of the emitted light can be tuned via gate voltage controlling the doping of the sample.

In 1986 H. Aoki proposed the first Landau-level laser for two-dimensional (2D) electron systems [1] exploiting the discreteness of the Landau levels (LLs) to tune the laser frequency through the magnetic field. The key challenge for the realization of such a LL laser is to obtain and to sustain a long-lived population inversion (PI) between LLs. This is difficult to achieve in conventional semiconductors where strong Coulomb scattering between equidistant LLs acts in favor of an equilibrium Fermi-Dirac distribution. Similarly, phonon-induced scattering can counteract PI, if the phonon energy is in resonance with the inter-Landau level transitions involved in the lasing process.

Graphene as a two-dimensional zero-gap semiconductor with remarkable properties [2–4] offers optimal conditions for LL lasing. Its linear electronic dispersion leads to an unconventional non-equidistant LL spacing including the appearance of a zero Landau level in an external magnetic field [5–7]. The observation of a number of interesting effects such as the fractional quantum Hall effect [8, 9], a giant Faraday rotation [10], the quantum ratchet effect [11], the Hofstadter butterfly [12–14], and the demonstration of a tunable THz detector [15] has already attracted enormous interest to Landau-quantized graphene [16]. The non-equidistant LLs and the specific optical selection rules allowing transitions between LLs with $n \rightarrow n \pm 1$ [17] make graphene an optimal material for the realization of an efficient two-dimensional LL laser. A transient population inversion in graphene without a magnetic field has already been theoretically predicted [18, 19] and experimentally demonstrated [20–22]. It emerges as a result of a relaxation bottleneck close to the Dirac point and decays mainly due to Coulomb-induced recombination processes [19].

In this article, we predict the occurrence of a long-lived population inversion in Landau-quantized graphene. We present two different experimentally feasible mechanisms to achieve the population inversion induced by optical

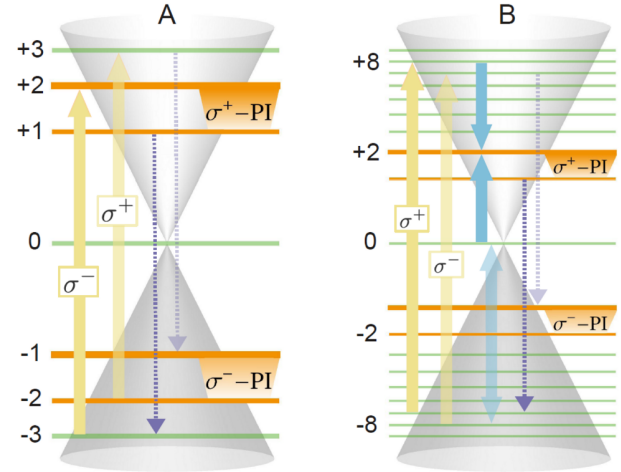


Figure 1. Two routes to population inversion (PI) in Landau-quantized graphene. The sketches show graphene's energetically lowest Landau levels (LLs) with the Dirac cone in the background. They illustrate different schemes to achieve population inversion between LL_{+1} and LL_{+2} (σ^+ -PI) and between LL_{-2} and LL_{-1} (σ^- -PI), respectively. Scheme A is based solely on optical pumping (indicated by the yellow arrows), which creates PI by populating LL_{+2} and depopulating LL_{-2} . Scheme B exploits efficient Auger scattering (cf. blue arrows) between the equidistant LLs +8, +2, and 0 to redistribute optically pumped electrons (holes) from LL_{+8} (LL_{-8}) to LL_{+2} (LL_{-2}). While the mechanism A is the basis for a three-LL laser system, the mechanism B involves a fourth level, which might be of advantage for the efficiency of such a laser. To allow for continuous laser action, phonon-assisted relaxation channels are needed that connect all LLs involved in the laser system (cf. purple-dotted arrows). The processes building up the σ^+ -PI in the conduction band are illustrated by bold arrows, while those giving rise to the σ^- -PI in the valence band are transparent.

pumping, cf. Fig. 1. The first mechanism (A) is based on the specific optical selection rules in Landau-quantized graphene yielding the possibility to selectively pump a single LL transition constituting an effectively three-level laser system, cf. Fig. 1A. The second mechanism (B) ex-

* florian.wendler@tu-berlin.de

exploits the scattering among electrons to achieve PI and thereby adds an additional level to the system, which can be beneficial for the efficiency of the laser, cf. Fig. 1B. Interestingly, scheme B provides a Coulomb-induced mechanism to create PI, which is quite remarkable, because Coulomb-induced Auger scattering was shown to rather reduce PI in graphene [19] and has been believed to be the main obstacle for the realization of a graphene-based two-dimensional LL laser [23]. Since we preserve the electron-hole symmetry, PI is obtained in the conduction band and in the valence band at the same time. It occurs between the LLs with the indices $n = 1$ and $n = 2$. However, we want to stress that also other schemes are possible to obtain PI for different LL transitions. Note that the PI transitions in the conduction and in the valence band are optically coupled by inversely circularly polarized photons, i.e. photons created in a stimulated emission process inducing the electronic transition $LL_{+2} \rightarrow LL_{+1}$ ($LL_{-1} \rightarrow LL_{-2}$) are σ^+ - polarized (σ^- - polarized). Hence, we label the corresponding population inversion as σ^+ - PI and σ^- - PI, respectively. The

proposed PI schemes A and B produce circular polarized photons with both rotational directions, which can be combined to produce linear polarized laser light.

With respect to future graphene-based applications, microscopic insights into the carrier dynamics in graphene are of crucial importance. While the relaxation channels without a magnetic field have been already thoroughly studied in experiment [22, 24–29] and theory [19, 29–33], the investigation of the carrier dynamics in Landau-quantized graphene has just started to pick up pace very recently [23, 34–38]. We have developed a theory based on the density matrix approach [32, 39] providing access to time and energy-dependent relaxation dynamics in Landau-quantized graphene and revealing microscopic insights into the underlying many-particle scattering pathways [36, 37]. The temporal evolution of LL carrier occupations $\rho_i = \langle a_i^\dagger a_i \rangle$ and microscopic polarizations $p_{ij} = \langle a_i^\dagger a_j \rangle$ (with the fermionic creation and annihilation operators a_i^\dagger and a_i) determining the strength of optical LL transitions is obtained using the graphene Bloch equations in the presence of a magnetic field

$$\dot{\rho}_i(t) = -2 \sum_j \text{Re}[\Omega_{ij}(t) p_{ij}(t)] + S_i^{\text{in}}(t) [1 - \rho_i(t)] - S_i^{\text{out}}(t) \rho_i(t), \quad (1)$$

$$\dot{p}_{ij}(t) = [i\Delta\omega_{ij} - \gamma(t)] p_{ij}(t) + \Omega_{ij}(t) [\rho_i(t) - \rho_j(t)]. \quad (2)$$

The set of coupled differential equations has been obtained by exploiting a correlation expansion within the second-order Born-Markov approximation [32, 39]. Here, we explicitly take into account the occupations and polarizations of the energetically lowest LLs up to $n = 10$, including the optical excitation as well as all energy-conserving carrier-carrier and carrier-phonon scattering processes. The introduced indices $i = (\xi_i, \lambda_i, n_i, m_i)$ are compound indices comprising the valley ξ_i , the band λ_i , the Landau level index n_i , and the quantum number m_i being connected to the centers of the cyclotron orbits in the graphene plane [16]. The Rabi frequency $\Omega_{ij} = \frac{e_0}{m_0} \mathbf{M}_{ij} \cdot \mathbf{A}(t)$ appearing in Eqs. 1 and 2 depends on the electron's charge e_0 , its free mass m_0 , the optical matrix element \mathbf{M}_{ij} [17], and on the vector potential $\mathbf{A}(t)$. The explicitly time-dependent scattering rates $S_i^{\text{in/out}}(t)$ incorporate all energy-conserving electron-electron and electron-phonon scattering processes including time-dependent Pauli blocking terms. The Coulomb interaction is dynamically screened taking into account the momentum dependence of the dielectric function in the random phase approximation [16, 37]. Phonon-induced scattering via the dominant optical phonon modes ΓTO , ΓLO , and KTO is taken into account, where a coupling to a bath is considered. The microscopic polarization decays due to a dephasing $\gamma(t)$ caused by many-particle scattering as well as

impurity-induced LL broadening. The energy difference $\Delta\omega_{ij} = (\epsilon_i - \epsilon_j)/\hbar$ between LL_i and LL_j describes the oscillation of the corresponding polarization. Excitonic effects are not considered, since they are known to be weak in the low-energy limit near the Dirac points of graphene [40, 41], which appears to be also valid under Landau-quantization, where no signatures of excitonic effects were observed in the low-energy regime [5, 7]. Furthermore, we assume an impurity-induced broadening of the LLs calculated in a self-consistent Born approximation [37, 42], where a reasonable strength of the impurity scattering is chosen [38, 43, 44] yielding a broadening of approximately 4 meV.

We investigate the carrier dynamics in graphene in the presence of an external magnetic field of $B = 4 \text{ T}$. We consider the system to be at room temperature with initial Fermi-Dirac distributed occupations that are optically excited by a pump pulse with a width of 1 ps, a pump fluence of $\epsilon_{\text{pf}} = 1 \mu\text{Jcm}^{-2}$, and an energy matching the pumped LL transitions of the respective PI scheme, cf. Fig. 1. In order to keep the excitation energy-dependent pulse area constant, the pump fluence in scheme B is increased to $\epsilon_{\text{pf}} = 2.27 \mu\text{Jcm}^{-2}$. Solving the graphene Bloch equations (Eqs. 1 and 2) yields the temporal evolution of the microscopic polarizations p_{ij} and of the LL occupations ρ_i allowing us to investigate the interplay between optical transitions on the one side and

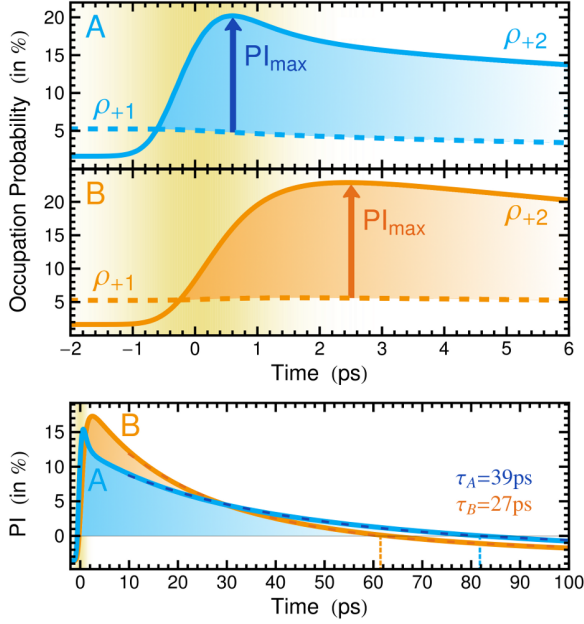


Figure 2. **LL occupations involved in the build-up of the population inversion.** The temporal evolution of the occupations ρ_{+1} and ρ_{+2} are shown in the upper panel for the PI schemes A and B (depicted in Fig. 1) illustrating the occurrence of a pronounced population inversion defined by $PI = \rho_{+2} - \rho_{+1} > 0$ (blue and orange shaded areas). The system is assumed to be at room temperature and under a magnetic field of $B = 4$ T. It is optically excited using a pulse with a width of 1 ps (cf. yellow area in the background) and a fluence of $\epsilon_{pf} = 1 \mu\text{Jcm}^{-2}$ in scheme A and $\epsilon_{pf} = 2.27 \mu\text{Jcm}^{-2}$ in scheme B to ensure the same pulse area. The lower panel shows the temporal evolution of the PI featuring an ultrafast build-up and a slow decay on a ps time-scale. Exponential fitting (dashed lines) reveals the corresponding decay times of $\tau_A = 39$ ps and $\tau_B = 27$ ps for both PI schemes. The vertical dashed lines mark the points in time where the PI vanishes ($PI = 0$) in the respective scheme.

carrier-carrier and carrier-phonon scattering processes on the other side. Since neutral Landau-quantized graphene is symmetric for electrons and holes, we focus the discussion on the σ^+ -PI in the conduction band. Figure 2 illustrates the time-dependent occupations of LL_{+1} and LL_{+2} (upper panel) as well as the resulting population inversion (lower panel). The qualitative behavior is the same in both PI schemes: While $\rho_{+1}(t)$ changes only slightly, $\rho_{+2}(t)$ shows a fast increase on a sub-picosecond time scale during and shortly after the optical excitation (illustrated by the yellow area in the background) followed by a slow decay on a picosecond time scale. We find a long-lived population inversion that is defined by

$$PI = \rho_{+2} - \rho_{+1} > 0 \quad (3)$$

and represented by the respective areas between ρ_{+1} and ρ_{+2} in Fig. 2. Exponential fits to the temporal evolutions of PI for schemes A and B (dashed lines in lower panel of Fig. 2) reveal their decay times $\tau_A = 39$ ps

and $\tau_B = 27$ ps. Since scheme A provides a straightforward approach to induce PI as a direct consequence of the optical excitation, the maximal value $PI_{\max}^A = 15.4\%$ is reached already during pumping. In scheme B, on the other hand, Coulomb-scattering is needed to induce PI by redistributing the optically excited charge carriers, consequently, the build-up time is longer and its maximum $PI_{\max}^B = 17.3\%$ is reached with a delay of a few picoseconds. While both PI schemes are suited to create a significant PI with a rather long decay time, the advantage of scheme B is its additional fourth level making it a potentially better laser system. This is reflected by its higher maximal PI value resulting from the fact that the optical excitation does not directly induce an enhanced occupation of the upper PI level LL_{+2} , but an additional level LL_{+8} is used (cf. Fig. 1). As a consequence, optically excited charge carriers in LL_{+8} scatter down to LL_{+2} already during pumping which reduces the pumping saturation and allows the excitation of more charge carriers. The cost of the enhanced maximal PI is a faster decay: In scheme A the PI vanishes after ~ 82 ps, while in scheme B the PI lasts ~ 62 ps. This can be explained by the more complex PI scheme B involving more LLs and therefore opening up more possible phonon-assisted decay channels reducing the PI (cf. Fig. 3).

To obtain more insights into the underlying elementary processes and to guide future experiments towards the demonstration of LL lasers, we investigate in the following the maximal PI as a function of experimentally accessible quantities, such as magnetic field strength, pump fluence, temperature, and doping. Figure 3 shows the dependence on the magnetic field for both PI schemes, where the thick lines represent the full dynamics, while the thin lines describe the dynamics without phonon-assisted scattering, and the dotted-thin lines taking into account only the impact of Γ TO-phonons. For this investigation, we determine the maximal PI at different magnetic fields B , while the pulse area is held constant by scaling the pump fluence linearly with the magnetic field. The energy of the PI transition $\epsilon_{+2} - \epsilon_{+1}$ is tunable via the magnetic field and is given on the upper axis. The dynamics without phonons (thin lines) shows a weak dependence on the magnetic field: At higher B , the LLs are shifted to higher energies, thereby reducing the initial occupations in the conduction band, in particular ρ_{+1} decreases resulting in a stronger PI. However, at the same time the scattering generally becomes more efficient with increasing magnetic fields, since the degeneracy of LLs scales with B . This enhances the dephasing $\gamma(t)$ of p_{ij} (cf. Eq. 2) and reduces the pumping efficiency and consequently also the maximal PI. These counteracting effects nearly balance each other out resulting in a very weak dependence on the magnetic field. Switching on phonon-induced scattering, the dependence qualitatively changes and pronounced peaks and dips emerge in the B -dependence of the maximal PI, cf. thick lines in 3. They indicate magnetic fields that fulfill the resonance condition between the energy of an optical phonon and

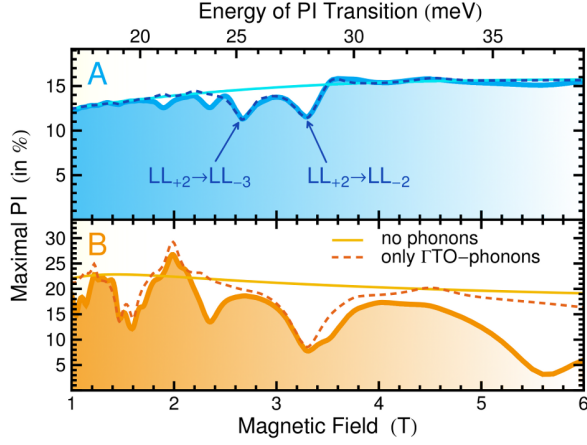


Figure 3. **Maximal population inversion as a function of magnetic field.** The dependence on the magnetic field is characterized by pronounced peaks and dips at resonant conditions, where an optical phonon energy matches the spacing between two Landau levels involved in the respective PI scheme. To illustrate this, the thin lines in A and B show the maximal PI, when electron-phonon scattering is switched off, and the dashed lines are obtained considering only ITO-phonons. In scheme A, two dips are present at $B = 2.67$ T and $B = 3.30$ T corresponding to resonances of the ITO-phonon energy with the transitions $LL_{+2} \rightarrow LL_{-3}$ and $LL_{+2} \rightarrow LL_{-2}$, respectively. In scheme B, three dips and two peaks appear and can be unambiguously ascribed to specific phonon-assisted LL transitions (cf. the text). In general, providing additional decay channels the carrier-phonon scattering reduces the PI. However, relaxation channels can also increase the PI, if they lead to a decrease of ρ_{+1} (lower PI level), an increase of ρ_{+2} (upper PI level), or if they populate LL_{-7} that increases the efficiency of pumping.

inter-Landau level transitions involved in the respective PI scheme. This is further evidenced by showing the dynamics that only includes ITO-phonons (dashed lines), where the number of peaks and dips is clearly reduced. In scheme A, two main resonances are present at the magnetic fields $B = 2.67$ T and $B = 3.30$ T. The first corresponds to the transition $LL_{+2} \rightarrow LL_{-3}$, while the second coincides with the transition $LL_{+2} \rightarrow LL_{-2}$, both reducing the PI by providing direct decay channels of the PI. The B -dependence in scheme B is more complex, since more LLs are involved (cf. Fig. 1) and hence more resonances occur. The three distinct dips at $B = 1.45$ T, $B = 1.60$ T, and $B = 3.30$ T correspond to the transitions $LL_{+2} \rightarrow LL_{-8}$, $LL_{+2} \rightarrow LL_{-7}$, and $LL_{+2} \rightarrow LL_{-2}$ (and at the same time $LL_{+8} \rightarrow LL_0$), respectively. For reasons of clarity, symmetric hole transitions are omitted for the discussion. Besides the decay of the PI similar to scheme A, phonons further reduce the PI in scheme B as they compete with the Coulomb channels, which are responsible for the appearance of the PI. Interestingly, phonon-induced scattering can also increase the PI, as can be seen at $B = 1.22$ T and $B = 1.99$ T. At these magnetic field strengths, the energy of the ITO-phonon

is in resonance with the transitions $LL_{+4} \rightarrow LL_{-7}$ and $LL_{+1} \rightarrow LL_{-7}$, respectively. The former case positively affects the pumping, while in the latter case the PI is not only increased through the depletion of LL_{+1} . It also couples the lower laser level LL_{+1} with the ground state LL_{-7} from which electrons are excited and thus connects the states of the four-level laser system (cf. Fig. 1). This opens up the possibility of continuous laser action in this system.

Besides the strength of the magnetic field, the pump fluence, the temperature, and the doping can be controlled in the experiment. To reveal the optimal conditions for a maximal population inversion, we perform further calculations investigating the impact of these externally accessible parameters, cf. Fig. 4. Since the optical excitation generates non-equilibrium carriers that fill up the upper gain level LL_{+2} , the PI increases with the pump fluence, cf. Fig. 4a. A saturation is reached when the optically excited LL becomes half filled, which hinders further pumping and imposes an upper limit to the PI. The initial thermal occupation of ρ_{+1} further decreases the maximal PI resulting in a saturation value of approximately 40% in scheme A and 45% in scheme B (not shown in the figure). The maximal PI at low fluences is slightly larger in scheme A, since the pulse area is larger in scheme A due to the lower frequency of the pump pulse. The higher saturation value of the PI in scheme B is a manifestation of the advantage of a four-level laser system compared to a three-level system in scheme A.

Furthermore, the PI is inversely correlated to the temperature T , i.e. the higher T the smaller is the population inversion, cf. Fig. 4b. At higher temperatures, the initial carrier occupation $\rho_{+1}(t_0)$ increases faster than $\rho_{+2}(t_0)$ resulting in a less pronounced PI, cf. Eq. 3. For temperatures less than 160 K the initial difference $\rho_{+1}(t_0) - \rho_{+2}(t_0)$ is below 0.5%, however it increases to 3.6% at room temperature and reaches 7.1% at $T = 500$ K which exactly reflects the predicted temperature dependence of the maximal PI. In scheme A, the effect is more pronounced, because the temperature also affects the LL occupations $\rho_{+2}(t_0)$ and $\rho_{+3}(t_0)$ that are involved in the optical excitation, whereas this effect is negligible in scheme B with the energetically high LL_{+8} and LL_{-7} .

Finally, doping opens up the possibility to control the PI by shifting the Fermi energy away from $E_F = 0$, which can be achieved by applying a gate voltage. This breaks the electron-hole symmetry and allows to tune the relative population inversion between the two inversely polarized LL transitions $LL_{\pm 2} \rightarrow LL_{\pm 1}$, cf. Fig. 4c. While a small positive Fermi energy gives rise to an increase of the σ^+ -PI, the impact on the σ^- -PI is opposite. This behavior can be attributed to new scattering channels that are forbidden under electron-hole symmetry, but arise as soon as this symmetry is broken. For simplicity, we focus on the simple PI scheme A in the following: An up-shift of the Fermi energy results in a less efficient

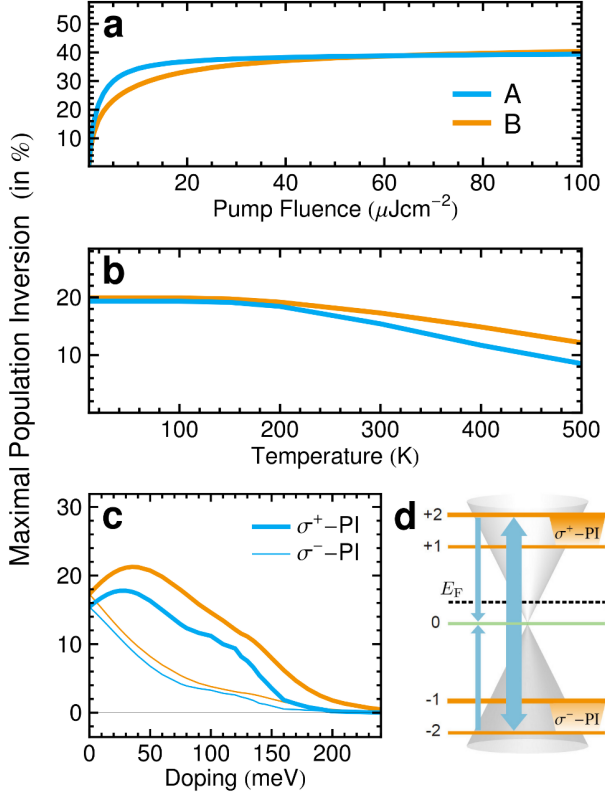


Figure 4. Maximal population inversion in dependence of pump fluence, temperature, and doping. The maximal PI between LL_{+1} and LL_{+2} is plotted as a function of (a) pump fluence, (b) temperature, and (c) doping. In the latter case, we also show the PI between LL_{-2} and LL_{-1} , since the electron-hole symmetry is broken once a doping is introduced. The sketch (d) illustrates the Coulomb-induced scattering (thick blue arrows) prevailing against its inverse process (thin blue arrows) that result in the asymmetry of the two PI transitions.

pumping of the transition $LL_{-3} \rightarrow LL_{+2}$ due to an enhanced Pauli blocking in comparison to the transition $LL_{-2} \rightarrow LL_{+3}$. According to this, σ^+ -PI should be suppressed, while σ^- -PI is expected to be enhanced. Interestingly, we observe the opposite behavior, as shown in Fig. 4. To understand the doping dependence, we consider the energy-conserving Coulomb process involving the transitions $LL_0 \rightarrow LL_{+2}$ and $LL_0 \rightarrow LL_{-2}$ (outward scattering), which is canceled out in an electron-hole symmetric system that also exhibits the inverse process (inward scattering: $LL_{+2} \rightarrow LL_0$ and $LL_{-2} \rightarrow LL_0$) occurring with the same probability. However, due to the asymmetric pumping and a more than half-filled LL_0 in a n-doped sample, the Coulomb-induced outward scattering prevails over the inward scattering, cf. Fig. 4d. As a result, σ^+ -PI is enhanced, while σ^- -PI is suppressed, as observed in Fig. 4c. Shifting the Fermi energy further away from the neutral position, the PI of both transitions decreases, which can be readily understood considering the initial occupations. When the Fermi energy reaches

the vicinity of LL_{+1} , its initial occupation $\rho_{+1}(t_0)$ is considerably increased counteracting the build-up of a population inversion. The values of the PI in both schemes show a similar dependence of the doping. A minor difference arises at ~ 100 meV and higher dopings, where the PI in scheme A does not decrease as fast as the PI in scheme B. Here, the Fermi energy takes similar values as the energy of LL_{+2} and the direct pumping into LL_{+2} in scheme A is beneficial, since Coulomb scattering from LL_{+8} to LL_{+2} in scheme B is strongly blocked in the beginning of pumping due to $\rho_{+8}(t_0) \ll \rho_{+2}(t_0)$.

In general, comparing both PI schemes (cf. Fig. 1), we find that they show a similar qualitative behavior. The PI rapidly builds up already during the excitation and slowly decays after the pump pulse on a time scale of few tens of ps (cf. Fig. 2). Furthermore, scheme B, describing a four-level laser system, is advantageous for continuous laser action. This is based on the fact that a resonance of an optical phonon energy with the transition $LL_{+1} \rightarrow LL_{-7}$ is feasible. This allows an electron to perform cycles in the four-level system: First it is excited from LL_{-7} to LL_{+8} , from where it scatters down and accumulates in LL_{+2} , before it participates in a stimulated emission event that transfers it to LL_{+1} . Now, a phonon with the appropriate energy can bring the electron back to LL_{-7} . The resonance condition is fulfilled for the GTO, FLO, and KTO-phonon modes at the magnetic fields $B = 1.99$ T, $B = 2.11$ T, and $B = 1.41$ T, respectively. A magnetic field of $B = 2$ T seems to be optimal, since no interfering resonances with other inter-LL transitions occur (cf. Fig. 3).

Finally, we propose a simple pump-probe experiment to test our predictions at sufficiently low temperatures, so that the initial occupations $\rho_{+1}(t_0)$ and $\rho_{+2}(t_0)$ are nearly zero: Exciting Landau-quantized graphene according to one of the PI schemes A or B, cf. Fig. 1, with a probe pulse measuring the σ^+ -PI absorption, a positive differential transmission signal (DTS) indicates a faster increase of ρ_{+2} in comparison to ρ_{+1} and consequently would provide strong evidence for the occurrence of gain.

In conclusion, based on microscopic calculations we predict the occurrence of a pronounced population inversion in Landau-quantized graphene and propose two different mechanisms to realize graphene-based LL lasers. Surprisingly, we show that carrier-phonon scattering, which generally reduces the population inversion, can be exploited to boost the effect and to even open the way to continuous wave laser operation. Furthermore, we demonstrate that the efficiency of the population inversion can be tuned via experimentally accessible quantities, such as the strength of the magnetic field and of the optical excitation. In particular, controlling the doping of the sample allows us to also tune the polarization of the emitted photons. Our microscopic insights into the carrier dynamics in Landau-quantized graphene can guide future experiments towards the design of graphene-based Landau level lasers or THz emitters.

ACKNOWLEDGMENTS

We acknowledge the financial support from the Einstein Stiftung Berlin and we are thankful to the DFG

for support through SPP 1459. Furthermore, we thank A. Knorr (TU Berlin), and S. Winnerl (Helmholtz-Zentrum Dresden-Rossendorf) for inspiring discussions on Landau-level lasers.

-
- [1] H. Aoki. Novel landau level laser in the quantum hall regime. *Appl. Phys. Lett.*, 48(9):559–560, 1986.
 - [2] K. S. Novoselov, A. K. Geim, S. V. Morozov, D. Jiang, Y. Zhang, S. V. Dubonos, I. V. Grigorieva, and A. A. Firsov. Electric field effect in atomically thin carbon films. *Science*, 306:666–669, 2004.
 - [3] Y. Zhang, Y.-W. Tan, H. L. Stormer, and P. Kim. Experimental observation of the quantum hall effect and berry’s phase in graphene. *Nature*, 438:201–204, 2005.
 - [4] A. K. Geim and K. S. Novoselov. The rise of graphene. *Nat. Mater.*, 6(3):183–191, 2007.
 - [5] M. L. Sadowski, G. Martinez, M. Potemski, C. Berger, and W. A. de Heer. Landau level spectroscopy of ultrathin graphite layers. *Phys. Rev. Lett.*, 97:266405, 2006.
 - [6] P. Plochocka, C. Faugeras, M. Orlita, M. L. Sadowski, G. Martinez, M. Potemski, M. O. Goerbig, J.-N. Fuchs, C. Berger, and W. A. de Heer. High-energy limit of massless dirac fermions in multilayer graphene using magneto-optical transmission spectroscopy. *Phys. Rev. Lett.*, 100:087401, 2008.
 - [7] M. Orlita, C. Faugeras, P. Plochocka, P. Neugebauer, G. Martinez, D. K. Maude, A.-L. Barra, M. Sprinkle, C. Berger, W. A. de Heer, and M. Potemski. Approaching the dirac point in high-mobility multilayer epitaxial graphene. *Phys. Rev. Lett.*, 101:267601, 2008.
 - [8] X. Du, I. Skachko, F. Duerr, A. Luican, and E. Y. Andrei. Fractional quantum hall effect and insulating phase of dirac electrons in graphene. *Nature*, 462:192–195, 2009.
 - [9] Kirill I. Bolotin, Fereshte Ghahari, Michael D. Shulman, Horst L. Stormer, and Philip Kim. Observation of the fractional quantum hall effect in graphene. *Nature*, 462:196–199, 2009.
 - [10] Iris Crassee, Julien Levallois, Andrew L. Walter, Markus Ostler, Aaron Bostwick, Eli Rotenberg, Thomas Seyller, Dirk van der Marel, and Alexey B. Kuzmenko. Giant faraday rotation in single- and multilayer graphene. *Nat. Phys.*, 7:48–51, 2011.
 - [11] C. Drexler, S. A. Tarasenko, P. Olbrich, J. Karch, M. Hirmer, F. Muller, M. Gmitra, J. Fabian, R. Yakimova, S. Lara-Avila, S. Kubatkin, M. Wang, R. Vajtai, P. M. Ajayan, J. Kono, and S. D. Ganichev. Magnetic quantum ratchet effect in graphene. *Nat. Nano.*, 8:104–107, 2013.
 - [12] L. A. Ponomarenko, R. V. Gorbachev, G. L. Yu, D. C. Elias, R. Jalil, A. A. Patel, A. Mishchenko, A. S. Mayorov, C. R. Woods, J. R. Wallbank, M. Mucha-Kruczynski, B. A. Piot, M. Potemski, I. V. Grigorieva, K. S. Novoselov, F. Guinea, V. I. Fal’ko, and A. K. Geim. Cloning of dirac fermions in graphene superlattices. *Nature*, 497:594–597, 2013.
 - [13] C. R. Dean, L. Wang, P. Maher, C. Forsythe, F. Ghahari, Y. Gao, J. Katoch, M. Ishigami, P. Moon, M. Koshino, T. Taniguchi, K. Watanabe, K. L. Shepard, J. Hone, and P. Kim. Hofstadter’s butterfly and the fractal quantum hall effect in moire superlattices. *Nature*, 497:598–602, 2013.
 - [14] B. Hunt, J. D. Sanchez-Yamagishi, A. F. Young, M. Yankowitz, B. J. LeRoy, K. Watanabe, T. Taniguchi, P. Moon, M. Koshino, P. Jarillo-Herrero, and R. C. Ashoori. Massive dirac fermions and hofstadter butterfly in a van der waals heterostructure. *Science*, 340:1427–1430, 2013.
 - [15] Yukio Kawano. Wide-band frequency-tunable terahertz and infrared detection with graphene. *Nanotechnol.*, 24:214004, 2013.
 - [16] M. O. Goerbig. Electronic properties of graphene in a strong magnetic field. *Rev. Mod. Phys.*, 83:1193–1243, 2011.
 - [17] K. M. Rao and J. E. Sipe. Coherent photocurrent control in graphene in a magnetic field. *Phys. Rev. B*, 86:115427, 2012.
 - [18] V. Ryzhii, M. Ryzhii, and T. Otsuji. Negative dynamic conductivity of graphene with optical pumping. *J. Appl. Phys.*, 101:083114, 2007.
 - [19] T. Winzer, E. Malić, and A. Knorr. Microscopic mechanism for transient population inversion and optical gain in graphene. *Phys. Rev. B*, 87:165413, 2013.
 - [20] T. Li, L. Luo, M. Hupalo, J. Zhang, M. C. Tringides, J. Schmalian, and J. Wang. Femtosecond population inversion and stimulated emission of dense dirac fermions in graphene. *Phys. Rev. Lett.*, 108:167401, 2012.
 - [21] S. Boubanga-Tombet, S. Chan, T. Watanabe, A. Satou, V. Ryzhii, and T. Otsuji. Ultrafast carrier dynamics and terahertz emission in optically pumped graphene at room temperature. *Phys. Rev. B*, 85:035443, 2012.
 - [22] Isabella Gierz, Jesse C. Petersen, Matteo Mitranio, Cephise Cacho, I. C. Edmond Turcu, Emma Springate, Alexander Stöhr, Axel Köhler, Ulrich Starke, and Andrea Cavalleri. Snapshots of non-equilibrium dirac carrier distributions in graphene. *Nature Mater.*, 12(12):1119–1124, 2013.
 - [23] P. Plochocka, P. Kossacki, A. Golnik, T. Kazimierczuk, C. Berger, W. A. de Heer, and M. Potemski. Slowing hot-carrier relaxation in graphene using a magnetic field. *Phys. Rev. B*, 80:245415, 2009.
 - [24] J. M. Dawlaty, S. Shivaraman, M. Chandrashekar, F. Rana, and M. G. Spencer. Measurement of ultrafast carrier dynamics in epitaxial graphene. *Appl. Phys. Lett.*, 92:042116, 2008.
 - [25] D. Sun, Z.-K. Wu, C. Divin, X. Li, C. Berger, W. A. de Heer, P. N. First, and T. B. Norris. Ultrafast relaxation of excited dirac fermions in epitaxial graphene using optical differential transmission spectroscopy. *Phys. Rev. Lett.*, 101:157402, 2008.
 - [26] S. Winnerl, M. Orlita, P. Plochocka, P. Kossacki, M. Potemski, T. Winzer, E. Malić, A. Knorr, M. Sprinkle, C. Berger, W. A. de Heer, H. Schneider, and M. Helm. Carrier relaxation in epitaxial graphene photoexcited near the dirac point. *Phys. Rev. Lett.*, 107:237401, 2011.

- [27] M. Breusing, S. Kuehn, T. Winzer, E. Malić, F. Milde, N. Severin, J. P. Rabe, C. Ropers, A. Knorr, and T. Elsaesser. Ultrafast nonequilibrium carrier dynamics in a single graphene layer. *Phys. Rev. B*, 83:153410, 2011.
- [28] J. C. Johannsen, S. Ulstrup, F. Cilento, A. Crepaldi, M. Zacchigna, C. Cacho, I. C. E. Turcu, E. Springate, F. Fromm, C. Raidel, T. Seyller, F. Parmigiani, M. Grioni, and P. Hofmann. Direct view of hot carrier dynamics in graphene. *Phys. Rev. Lett.*, 111:027403, 2013.
- [29] D. Brida, A. Tomadin, C. Manzoni, Y. J. Kim, A. Lombardo, S. Milana, R. R. Nair, K. S. Novoselov, A. C. Ferrari, G. Cerullo, and M. Polini. Ultrafast collinear scattering and carrier multiplication in graphene. *Nature Commun.*, 4:1987, 2013.
- [30] F. Rana. Electron-hole generation and recombination rates for coulomb scattering in graphene. *Phys. Rev. B*, 76:155431, 2007.
- [31] T. Winzer, A. Knorr, and E. Malic. Carrier Multiplication in Graphene. *Nano Lett.*, 10:4839–4843, 2010.
- [32] E. Malic and A. Knorr. *Graphene and Carbon Nanotubes: Ultrafast Optics and Relaxation Dynamics*. Wiley-VCH, 2013.
- [33] Faris Kadi, Torben Winzer, Ermin Malic, Andreas Knorr, F. Göttfert, M. Mittendorff, S. Winnerl, and M. Helm. Microscopic description of intraband absorption in graphene: The occurrence of transient negative differential transmission. *Phys. Rev. Lett.*, 113:035502, 2014.
- [34] W.-P. Li, J.-W. Yin, Y.-F. Yu, and Z.-W. Wang. Two-phonon relaxation processes of the graphene in the magnetic field. *Solid State Commun.*, 163:19 – 22, 2013.
- [35] Z.-W. Wang, L. Liu, L. Shi, X.-J. Gong, W.-P. Li, and K. Xu. The temperature dependence of optical phonon scattering in graphene under strong magnetic field. *J. Phys. Soc. Jpn.*, 82:094606, 2013.
- [36] Florian Wendler, Andreas Knorr, and Ermin Malic. Resonant carrier-phonon scattering in graphene under landau quantization. *Appl. Phys. Lett.*, 103(25):253117, 2013.
- [37] Florian Wendler, Andreas Knorr, and Ermin Malic. Carrier multiplication in graphene under landau quantization. *Nature Commun.*, 5:3703, 2014.
- [38] M. Mittendorf, F. Wendler, E. Malic, A. Knorr, M. Orlita, M. Potemski, C. Berger, W. A. de Heer, H. Schneider, M. Helm, and S. Winnerl. Ultrafast carrier dynamics in landau-quantized graphene: strong auger scattering. (*accepted by Nat. Phys.*), 2014.
- [39] H. Haug and S. W. Koch. *Quantum Theory of the Optical and Electronic Properties of Semiconductors*. World Scientific, 2009.
- [40] D.-H. Chae, T. Utikal, S. Weisenburger, H. Giessen, K. v. Klitzing, M. Lippitz, and J. Smet. Excitonic fano resonance in free-standing graphene. *Nano Lett.*, 11:1379–1382, 2011.
- [41] K. F. Mak, J. Shan, and T. F. Heinz. Seeing many-body effects in single- and few-layer graphene: Observation of two-dimensional saddle-point excitons. *Phys. Rev. Lett.*, 106:046401, 2011.
- [42] T. Ando. Theory of quantum transport in a two-dimensional electron system under magnetic fields. i. characteristics of level broadening and transport under strong fields. *J. Phys. Soc. Jpn.*, 36:959–967, 1974.
- [43] Nguyen Hong Shon and Tsuneya Ando. Quantum transport in two-dimensional graphite system. *J. Phys. Soc. Jpn.*, 67(7):2421–2429, 1998.
- [44] Justin C. W. Song, Michael Y. Reizer, and Leonid S. Levitov. Disorder-assisted electron-phonon scattering and cooling pathways in graphene. *Phys. Rev. Lett.*, 109:106602, 2012.